

Development and validation of a reflectance-based approach for oxygen saturation estimation using high-speed hyperspectral imaging

Cyrus Ngan^{a,b}, Kelden Pruitt^{a,b}, Baowei Fei^{a,b,c}*

^a University of Texas at Dallas, Department of Bioengineering, Richardson, TX;

^b University of Texas at Dallas, Center for Imaging and Surgical Innovation, Richardson, TX;

^c University of Texas Southwestern Medical Center, Department of Radiology, Dallas, TX

* Corresponding author: bfei@utdallas.edu, Website: <https://fei-lab.org>

ABSTRACT

During image-guided surgery and anastomosis procedures, it is important to monitor physiological status and assess tissue perfusion. Hyperspectral imaging (HSI) can be used to estimate superficial tissue oxygen saturation (sO_2), where native reflectance measurements are converted to absorbance for spectral unmixing and sO_2 estimation. However, keeping the reflectance data in its native form may improve accuracy. We developed a reflectance-based approach for sO_2 estimation with a high-speed HSI system, leveraging band-filtering and data processing techniques to improve performance. Our approach is validated with blood oxygenation and tissue-mimicking phantoms, utilizing a blood-gas analyzer (BGA) to obtain ground-truth measurements. The reflectance-based approach achieved a median error of 5.0% and 5.3% with the blood oxygenation and tissue-mimicking phantoms, respectively, effectively halving the error achieved with an absorbance-based approach (10.4%). Overall, we present a novel reflectance-based approach for sO_2 estimation that achieves superior performance compared to a conventional absorbance-based technique. Paired with high-speed HSI and robust BGA validation, this approach offers strong potential for clinical translation. Thus, the reflectance-based HSI sO_2 estimation approach can have many applications in image-guided surgery and interventional procedures.

Keywords: Hyperspectral imaging, oxygen saturation, spectral unmixing, image-guided surgery

1. INTRODUCTION

Superficial tissue oxygen saturation (sO_2) measurement is an important application of hyperspectral imaging (HSI) and allows surgical professionals to assess tissue perfusion behavior for critical procedures like wound healing evaluation [1, 2] and anastomosis [3]. Currently, a few systems have been developed for sO_2 visualization, including a commercial flexible endoscopic device that utilizes white light imaging to estimate tissue oxygenation. Although these have demonstrated clinical feasibility [1, 4], they face several limitations regarding capture speed and data accuracy. Current systems can require up to seven seconds to capture and analyze an image under standard settings [5], resulting in delays and increasing risk for inaccuracies caused by conditions like lighting and motion blur. In addition to acquisition speeds, these systems introduce additional complexity by converting natively captured reflectance data to absorbance values before estimating sO_2 levels, which may hinder overall estimation accuracy [6]. Furthermore, systems primarily depend on data gathered in the visible wavelength range (VIS, 400-700 nm) [7] where measured reflectance from hemoglobin is relatively low due to high absorption. Finally, publicly available validation practices also remain limited, with some systems relying on topical near-infrared spectroscopy devices that may not provide optimum reliability [6].

High-speed snapshot HSI systems have been demonstrated to alleviate the limitations associated with long acquisition times in push-broom systems [8], suggesting the potential for real-time sO_2 visualization. Our work seeks to develop a reflectance-based oxygen saturation estimation algorithm compatible with high-speed HSI and to evaluate its performance against a conventional absorbance-based unmixing approach. Multiple hyperspectral cameras were utilized to assess estimation accuracy in different wavelength ranges, and robust validation was performed with oxygenation phantoms, with ground-truth measurements obtained from a clinical blood-gas analyzer (BGA).

2. MATERIALS AND METHODS

2.1 Oxygen saturation estimation

Tissue sO_2 calculations depend on relative, or absolute, concentrations of deoxyhemoglobin (HbR) and oxyhemoglobin (HbO_2), which can be measured optically due to their distinct absorption behaviors. We utilized an optical window of 460–960 nm to estimate relative endmember concentrations, as this range contains known absorbance deviations of both hemoglobin forms [9]. With the relative concentrations of each, sO_2 can be calculated according to Equation 1.

$$sO_2 = \frac{[HbO_2]}{[HbO_2] + [HbR]} \quad (1)$$

As a benchmark, a conventional absorbance-based approach was implemented by converting HSI reflectance data into absorbance using the Dahm equation [10], followed by linear unmixing based on a modified Beer-Lambert equation. In contrast, our reflectance-based technique maintains the simplicity of linear unmixing, but retains the natively acquired measurements using derived *reflectance* coefficients in place of well-known absorption coefficients.

To perform spectral unmixing, HbO_2 and HbR absorption coefficient values were obtained [11] and normalized to the maximum value over the wavelength range captured by the respective hyperspectral (HS) camera. In order to convert these normalized absorption coefficients to reflectance coefficients, the Dahm equation was rearranged as follows:

$$A \approx -\log(R) \rightarrow r \approx 10^{-\tilde{a}} \quad (2)$$

where absorbance, A , is substituted for normalized absorption coefficients, \tilde{a} , and reflectance, R , is substituted for the reflectance coefficients, r . Once reflectance coefficients are determined for each endmember, linear unmixing is performed on the reflectance data from isosbestic-normalized HS images. Spectral unmixing was performed in MATLAB® (R2025a, The MathWorks, Natick, MA, USA) using the *lsqnonneg* function. In tissue-mimicking phantoms that included intralipid, fat was included as an additional endmember, with absorption coefficients obtained by Van Veen et al. [12].

Wavelength removal and R^2 -filtering

To investigate further improvements in sO_2 estimation accuracy, band reduction techniques were developed and evaluated, including manual and signal-to-noise (SNR) removal. Manual band removal was performed by isolating the 600 – 810 nm range, as it showed the most pronounced differences in hemoglobin optical behavior. SNR band reduction was performed by removing bands that failed to reach a predetermined SNR threshold, as defined by the following equation:

$$SNR_\lambda = \frac{\mu_{ROI}}{\sigma_{ROI}} \quad (3)$$

where μ is the mean intensity over a region of interest (ROI) at wavelength λ and σ is the standard deviation over the same region. Calculated sO_2 values were further processed based on the quality of the linear unmixing with a pixelwise R^2 -filter, calculated between the original HS and reconstructed reflectance signatures. Individual pixels with R^2 values that fell below set thresholds were eliminated from the final sO_2 estimation. Thresholds of interest included 0.8, 0.7, 0.6, and 0.5.

2.2 Oxygenation phantoms

Validation of the proposed algorithm was performed by comparing measurements from a clinical BGA (Stat Profile® Prime Plus, Nova Biomedical, MA) to HSI estimations in two phantom studies: a blood oxygenation phantom and a tissue-mimicking oxygenation phantom. Both phantoms utilized defibrinated whole porcine blood, as its physiological properties are similar to those of human blood [13]. Samples drawn directly from the stock container were considered fully oxygenated, as confirmed by BGA measurements, and were chemically deoxygenated with sodium dithionite ($Na_2S_2O_4$, NaD) dissolved in phosphate-buffered saline (PBS) solution. All PBS solution was sparged with nitrogen gas for 30 minutes to remove dissolved oxygen prior to its use.

Blood oxygenation studies

Blood oxygenation studies used an 18 mg/mL NaD solution to create six graded NaD concentrations per trial, with serial dilutions ranging from 0.0 mg/mL to 2.0 mg/mL. Table 1 displays the volumes of each component included to reach the desired concentrations. The resulting solutions were added to 4.5 mL of blood by pipetting both components into labelled 8.0 mL sterile test tubes, as shown in Figure 1(a). The final tube was capped, mixed with gentle inversions to avoid bubble artifacts, and brought to room temperature via palmar warmth. A seventh tube was established to obtain a control value for the BGA. Prior to imaging, each tube was carefully poured into the corresponding labelled 5-mL well, as shown in Figure 1(b), where 135 μ L of contents were extracted by the BGA for analysis.

Table 1. Components of the serially diluted sodium dithionite solutions by sample.

Tube	PBS	NaD Solution	mg NaD/ mL Blood
1	0.5 mL	0.0 mL	0.0 mg/mL
2	0.4 mL	0.1 mL	0.4 mg/mL
3	0.3 mL	0.2 mL	0.8 mg/mL
4	0.2 mL	0.3 mL	1.2 mg/mL
5	0.1 mL	0.4 mL	1.6 mg /mL
6	0.0 mL	0.5 mL	2.0 mg/mL

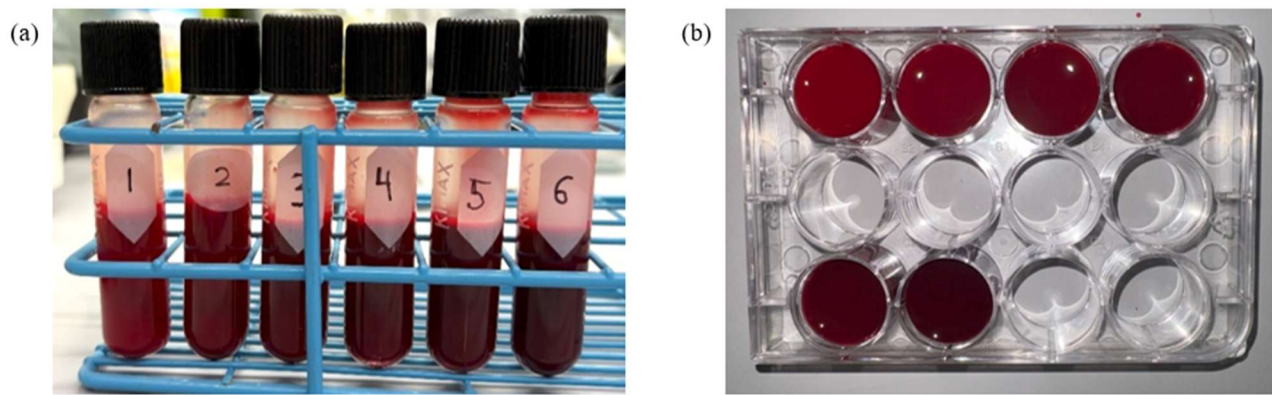


Figure 1. Stages of blood oxygenation phantom creation process. (a) Defibrinated porcine blood and graded Na₂S₂O₄ solution mixture are created in labelled test tubes. (b) Phantoms poured out into 10-mL wells for sampling and imaging.

Tissue-mimicking oxygenation phantoms

Chemical deoxygenation for the tissue-mimicking phantoms was performed similarly with a NaD stock concentration of 12 mg/mL. Furthermore, the phantoms included additional components to simulate human tissue, including a 1.42% v/v agar solution and a 20% v/v intralipid solution to mimic optical scattering behaviors. The agar solution consisted of agar and PBS, with glycerol for stability, and was gradually heated with procedural stirring until it became clear. The intralipid solution consisted of soybean oil, polysorbate-80 as the phospholipid, PBS, and glycerin, and was sonically emulsified. To avoid protein denaturation, all solutions were cooled to 40 °C prior to fabrication [14] with an active stir rod to prevent premature curing. Like the blood oxygenation phantoms, a small amount of the blood solution was extracted by the BGA before its addition to the final phantom. Phantom constituents consisted of 25% porcine blood, 66% agar solution, 5% intralipid solution, and 4% NaD solution, with fabrication results displayed in Figure 2.

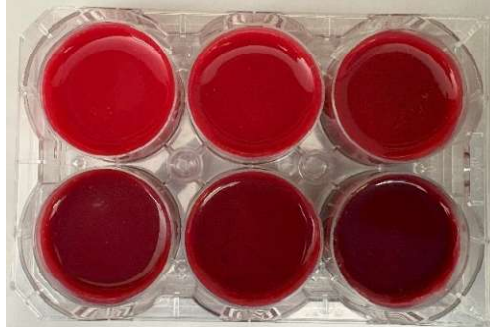


Figure 2. Final tissue-mimicking oxygenation phantoms following fabrication and imaging.

2.3 Data acquisition and analysis

HS images were acquired using a similar setup to our previous work [15] that captures images in the visual (VIS, 460 – 600 nm), red/near-infrared (RNIR, 600 – 870 nm), and near-infrared (NIR, 660 – 960 nm) spectral ranges. Estimations and evaluations of sO_2 were isolated by camera to identify optimal optical windows. Blood oxygenation and tissue-mimicking phantom trials were conducted ten and four times, respectively. ROIs were manually selected to avoid glare.

The primary metric used for analysis was absolute error, as determined between estimation values and corresponding BGA measurements. Technical replicates were averaged within each sample. Overall statistical comparisons across conditions were evaluated with Friedman tests. Significance was determined at $\alpha = 0.05$, with Bonferroni correction applied to account for comparisons within the processed datasets. For conditions indicating significance, post hoc Wilcoxon signed-rank tests were performed to assess pairwise differences.

3. RESULTS

3.1 Dataset Composition

A total of ten blood oxygenation phantom trials were completed, two of which were later removed from further analysis due to procedural errors. As each trial contained six varied sO_2 samples, a total of 48 sO_2 samples were fabricated and imaged over a range of 26–100%, as measured by the BGA and displayed by Figure 3. These values establish ground truth measurements for later analysis. In addition, four tissue-mimicking phantom trials were conducted and demonstrated sO_2 distribution ranging from 5.5–100%. All samples were imaged with three technical replicates for additional precision.

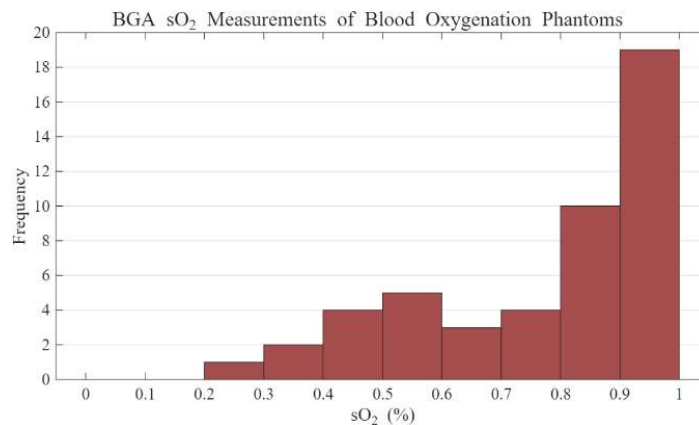


Figure 3. Histogram displaying sO_2 levels achieved among 48 blood oxygenation phantom samples from eight trials, as determined by BGA measurements.

3.2 Blood Oxygenation Phantom Results

Absorbance and reflectance-based sO_2 estimations were made for all blood oxygenation phantom trials. Figure 4 shows the comparison of results achieved between each method without any HS image processing. With the exception of the RNIR data, minimal differences were observed between the two approaches. Notably, the VIS camera produced the least accurate measurements of the three cameras. In fact, the performance of the VIS camera was unaffected by additional HS image processing methods (band reduction or pixelwise filtering). As such, subsequent analysis was carried out for the RNIR and NIR cameras.

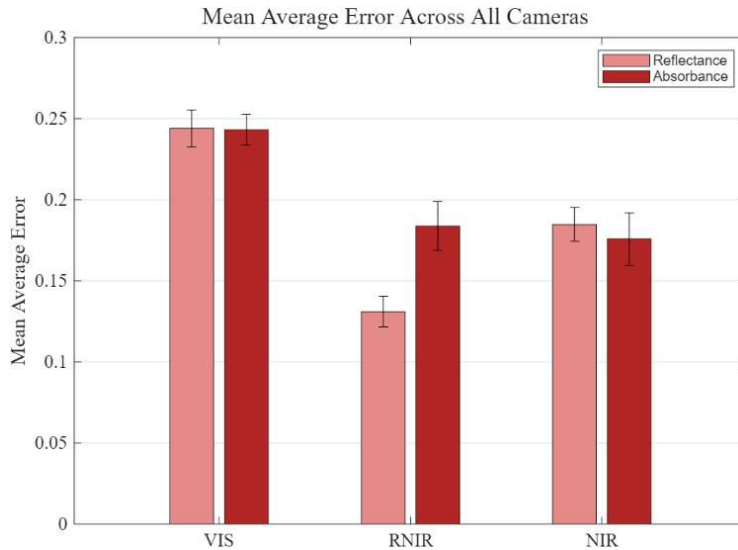


Figure 4. Mean average error across all cameras for all 48 samples without wavelength removal or R^2 filtering techniques, calculated by the difference between estimated and BGA values. Standard errors of mean are displayed.

Figure 5 displays the influence of each band reduction technique on the resulting errors across the blood oxygenation phantoms. Initial Friedman tests returned significant for each combination of camera and approach, warranting post hoc testing. Overall, the reflectance-based estimations were superior to absorbance-based estimations. In particular, our approach excelled when paired with SNR band reduction, demonstrated by the significant improvements in the RNIR data (median error of 0.07) over manual and no removal results. Similarly, estimations performed on NIR data resulted in significant improvement with the addition of either band removal technique (SNR and manual), achieving the lowest median error of 0.05.

Additionally, pixelwise filtering was performed via R^2 -filtering at thresholds of 0.8, 0.7, 0.6, and 0.5. Friedman tests indicated significance for each camera, with results from post-hoc Wilcoxon tests for pairwise evaluations shown in Figure 6. No significant differences between any two groups were noted in the NIR estimations, although a slight trend was present in the RNIR dataset estimations, indicating superior performance at lower thresholds.

3.3 Tissue-Mimicking Phantom Results

A total of four tissue-mimicking oxygenation phantom trials were imaged and analyzed. Figure 7 displays the performance differences between unmixing groups achieved with the reflectance-based approach, paired with SNR filtering and an R^2 -filter threshold of 0.5. Notably, the RNIR dataset indicated a significant difference ($p = 0.004$) when fat was introduced as an endmember for unmixing. While not statistically significant ($p = 0.563$), the NIR dataset suggested similar trends with a lower MAE achieved by the fat-included unmixing estimation.

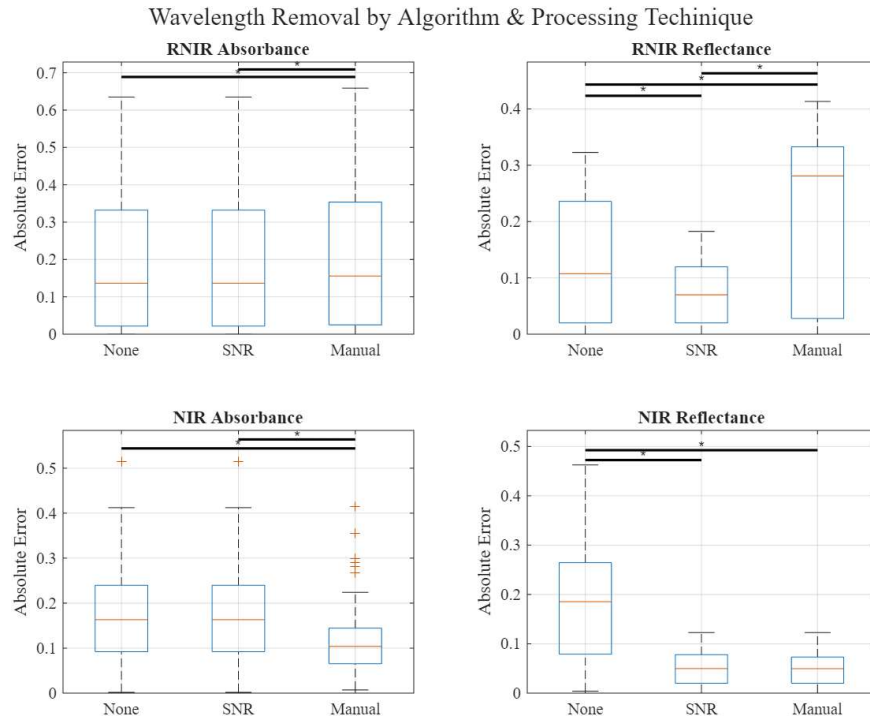


Figure 5. Boxplots of absolute errors across RNIR and NIR cameras, absorbance and reflectance-based approaches, and band removal techniques. Asterisks indicate significance with p-values less than $\alpha = 0.05$.

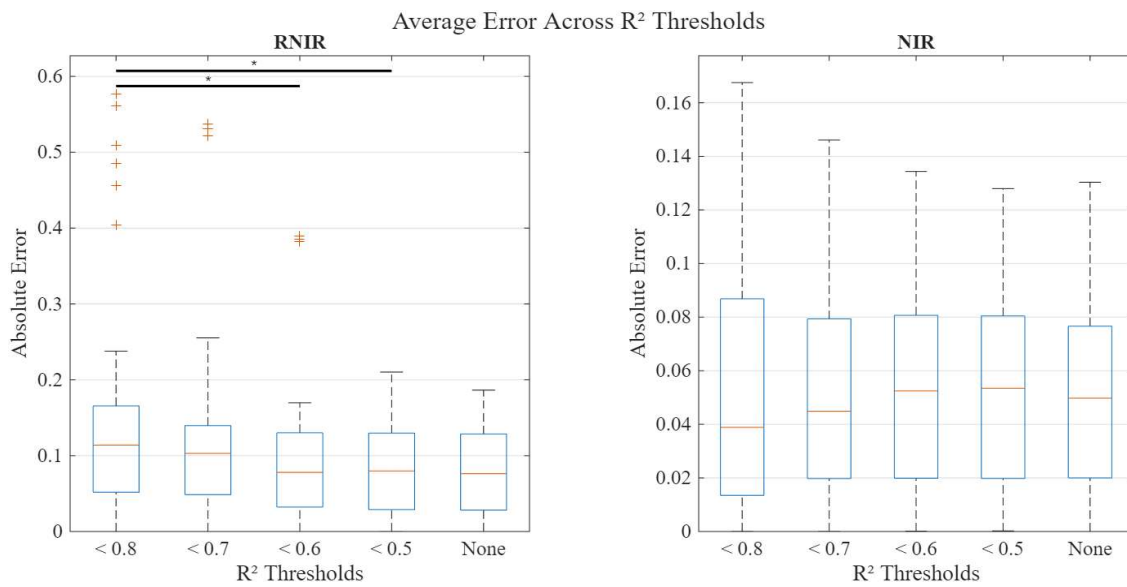


Figure 6. Absolute errors achieved with SNR band reduction and R^2 -filtering at thresholds of 0.5, 0.6, 0.7, and 0.8. "None" indicates performance without pixel removal. Asterisks indicate comparisons with p-values less than $\alpha = 0.05$.

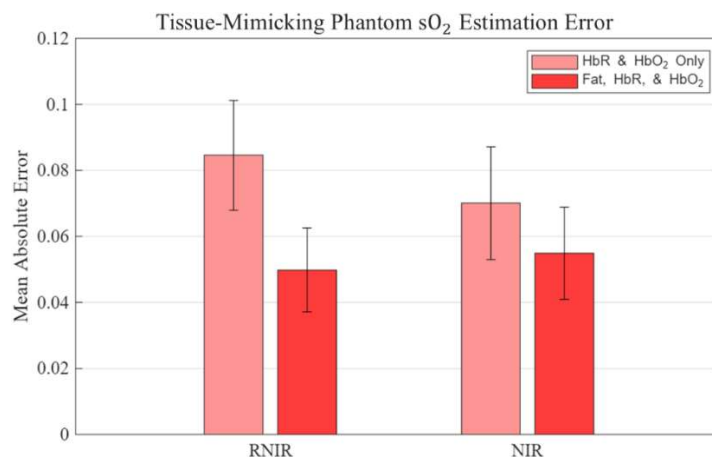


Figure 7. Comparison of MAE achieved by inclusion of fat as an endmember in the spectral unmixing compared to the simpler, hemoglobin-only unmixing. Results shown for both the RNIR and NIR cameras.

4. DISCUSSION AND CONCLUSIONS

We present a novel reflectance-based approach for sO₂ estimation that has the potential to advance optical oxygenation estimation methods using HSI. We addressed the limitations of slow acquisition speeds in current imaging systems by implementing a snapshot HSI system and simplified the estimation procedure by performing sO₂ estimation calculations on native reflectance data. To improve overall accuracy, we used band reduction techniques and R²-filtering, highlighting the performance of data acquired in the RNIR/NIR optical window over the conventional VIS spectral range. Finally, we developed a robust validation approach utilizing clinical BGA measurements in blood oxygen studies and tissue-mimicking phantoms. Our results demonstrated that the reflectance-based estimation achieved superior accuracy compared to traditional absorbance-based estimations, underscoring its potential to refine conventional optical oxygenation estimation approaches with HSI.

With high-speed HSI systems and image processing algorithms that account for the dynamic nature of blood and tissue, real-time tissue oxygenation measurements can enhance the performance of surgical procedures that rely on the accurate mapping of perfused areas. Future work will explore additional processing and filtering techniques to improve the accuracy and efficiency of optical sO₂ estimations, advancing toward vivo studies and clinical translation. Additionally, further refinement of the oxygenation phantom procedure may improve the distribution of actual sO₂ values, allowing for a more comprehensive evaluation of the algorithm across the full range of tissue sO₂ states.

ACKNOWLEDGEMENTS

Research reported in this publication was supported in part by the National Cancer Institute of the National Institutes of Health under Award Number R01CA288379 and by the Cancer Prevention and Research Institute of Texas (CPRIT) under Award Number RP240289 and RP240542. The content is solely the responsibility of the authors and does not necessarily represent the official views of the National Institutes of Health.

REFERENCES

- [1] A. Merdasa *et al.*, "Oxygen saturation mapping during reconstructive surgery of human forehead flaps with hyperspectral imaging and spectral unmixing," (in eng), *Microvascular research*, vol. 150, p. 104573, Nov 2023, doi: 10.1016/j.mvr.2023.104573.
- [2] Y.-S. Shin, K.-S. Hung, C.-T. Tsai, M.-H. Wu, C.-L. Lin, and Y.-Y. Hsueh, "Validation of multispectral imaging-based tissue oxygen saturation detecting system for wound healing recognition on open wounds," *Journal of Biomedical Optics*, vol. 29, no. 8, p. 086004, 2024. [Online]. Available: <https://doi.org/10.1117/1.JBO.29.8.086004>.

- [3] B. Jansen-Winkel *et al.*, "Determination of the transection margin during colorectal resection with hyperspectral imaging (HSI)," *International Journal of Colorectal Disease*, vol. 34, no. 4, pp. 731-739, 2019, doi: 10.1007/s00384-019-03250-0.
- [4] S. Kamba, M. Rugivarodom, A. Storm, L. W. Kee Song, and E. Rajan, "Feasibility study of real-time oxygen saturation endoscopic imaging (oxei) technology during endoluminal suturing of large mucosal defects in a porcine model," *Gastrointestinal Endoscopy*, vol. 99, no. 6, p. AB769, 2024, doi: 10.1016/j.gie.2024.04.1839.
- [5] M. T. Thomaßen *et al.*, "In vivo evaluation of a hyperspectral imaging system for minimally invasive surgery (HSI-MIS)," (in eng), *Surg Endosc*, vol. 37, no. 5, pp. 3691-3700, May 2023, doi: 10.1007/s00464-023-09874-2.
- [6] A. Holmer, J. Marotz, P. Wahl, M. Dau, and P. W. Kämmerer, "Hyperspectral imaging in perfusion and wound diagnostics - methods and algorithms for the determination of tissue parameters," *Biomed Tech (Berl)*, vol. 63, no. 5, pp. 547-556, Oct 25 2018, doi: 10.1515/bmt-2017-0155.
- [7] M. Alomari, I. Wadiwala, S. Bowers, E. F. Elli, and M. Thomas, "Oxygen Saturation Endoscopic Imaging as a Novel Alternative to Assess Tissue Perfusion During Esophagectomy," *Surgical Innovation*, vol. 31, no. 6, pp. 622-626, 2024, doi: 10.1177/15533506241290071.
- [8] K. Pruitt *et al.*, "Design and validation of a high-speed hyperspectral laparoscopic imaging system," *Journal of Biomedical Optics*, vol. 29, no. 9, p. 093506, 2024. [Online]. Available: <https://doi.org/10.1117/1.JBO.29.9.093506>.
- [9] S. L. Jacques, "Corrigendum: Optical properties of biological tissues: a review," *Physics in medicine and biology*, vol. 58, no. 14, pp. 5007-5008, 2013, doi: 10.1088/0031-9155/58/14/5007.
- [10] K. D. Dahm and D. J. Dahm, "Separating the Effects of Scatter and Absorption Using the Representative Layer," *J. Near Infrared Spectrosc.*, vol. 21, no. 5, pp. 351-357, 2013. [Online]. Available: <https://opg.optica.org/jnirs/abstract.cfm?URI=jnirs-21-5-351>.
- [11] S. Prahl. "Visible Human Hemoglobin Spectra." Oregon Medical Laser Center (OMLC). <https://omlc.org/spectra/hemoglobin/> (accessed 2025-06-12, 2025).
- [12] R. L. Van Veen, H. J. Sterenborg, A. Pifferi, A. Torricelli, E. Chikoidze, and R. J. J. o. b. o. Cubeddu, "Determination of visible near-IR absorption coefficients of mammalian fat using time-and spatially resolved diffuse reflectance and transmission spectroscopy," vol. 10, no. 5, pp. 054004-054004-6, 2005.
- [13] N. Koomkrong, C. Boonkaewwan, W. Laenoi, and A. Kayan, "Blood haematology, muscle pH and serum cortisol changes in pigs with different levels of drip loss," *Asian-Australasian journal of animal sciences*, vol. 30, no. 12, pp. 1751-1755, Dec 2017, doi: 10.5713/ajas.17.0037.
- [14] M. Kim *et al.*, "Fabrication of agar-based tissue-mimicking phantom for the technical evaluation of biomedical optical imaging systems," *Current Applied Physics*, vol. 61, pp. 80-85, 2024, doi: 10.1016/j.cap.2024.02.013.
- [15] K. Pruitt, W. DeAtley, A. Rathgeb, B. Johnson, J. Gahan, B. Fei, "A high-speed hyperspectral imaging system and large-scale hyperspectral dataset for abdominal surgical applications," Proc. SPIE 13408, Medical Imaging 2025: Image-Guided Procedures, Robotic Interventions, and Modeling, 134080B (7 April 2025); <https://doi.org/10.1117/12.3048439>.